# Representing anthropogenic dust in E3SMv1: Implementation, evaluation, and assessment of their radiative forcing

Yang Shi[1*], Xiaohong Liu[1], Chenglai Wu[2], Zheng Lu[1], Kai Zhang[3], and Po-Lun Ma[3]

[1]Department of Atmospheric Sciences, Texas A&M University, College Station, TX, USA
[*]Now at Department of Civil and Environmental Engineering, Massachusetts Institute of Technology, Cambridge, TX, USA
[2]International Center for Climate and Environment Sciences, Institute of Atmospheric Physics, Chinese Academy of Sciences, Beijing, China
[3]Atmospheric Sciences and Global Change Division, Pacific Northwest National Laboratory, Richland, Washington, USA

*Correspondence to*: Xiaohong Liu (xiaohong.liu@tamu.edu)

**Key Points:**

- An anthropogenic dust emission parameterization is developed and implemented in a global climate model.
- Our parameterization predicts that 13.3% of the total dust emission in present day is anthropogenic dust emission.
- Total dust emission increases by 13% from pre-industrial to present day, which results in a dust direct radiative forcing of -0.041 W $m^{-2}$.

**Key words:**

Anthropogenic dust emission, dust radiative forcing

**Abstract**

Dust emissions related to anthropogenic activities (i.e., anthropogenic dust (AD)) is not represented in most global climate models and its radiative impact remains unassessed. In this study, we develop a new and physically based method to parameterize AD emission based on the DOE's Energy Exascale Earth System Model version 1 (E3SMv1). This method relates AD emission to the crop land use fraction in the E3SMv1 land component. Major AD sources simulated by our parameterization include those over Central America, the Sahel, North India, and North China. The annual averaged AD emission is 567 Tg $yr^{-1}$ in present-day (year 2000), which contributes to 13.3 % of total dust emission. Model evaluation against satellite and ground-based observations shows that the new parameterization can represent AD emissions and global dust cycle reasonably well. We find that the total dust emission increases by 13 % (495 Tg $yr^{-1}$) from 1850 to 2000 mainly due to the cropland land use fraction changes, which induces a net dust direct effective radiative forcing of -0.041 W $m^{-2}$ at top of the atmosphere. This AD-induced cooling exceeds 10% of the total anthropogenic aerosol direct effective radiative forcing from 1750 to 2014 estimated by the Intergovernmental Panel on Climate Change Sixth Assessment Report. Our findings indicate an important role of AD in the regional and global climate changes, which should be included in future climate change assessments.

## Plain Language Summary

Dust aerosols are generally recognized as natural aerosols whose atmospheric burden remains stable with time. However, studies have found that anthropogenic activities can also induce dust emissions. Anthropogenic dust (AD) emission is not represented in most global climate models, and its impact on climate is not well understood. In this study, we implement an AD emission parameterization in a global climate model that physically relates AD emission to cropland fraction. Our modelling results show that 13.3% global dust emission in the present day is from AD sources, which includes those over Central America, the Sahel, North India, and North China. Due to agricultural expansion, total dust emission increases by 13% from pre-industrial to present day, which is dominated by the increase in AD emission. This historical increase results in cooling effect of dust on climate through scattering and absorbing radiation, which exceeds 10% of the estimate by the Intergovernmental Panel on Climate Change Sixth Assessment Report. Our findings indicate an important role of AD in the global climate changes, which should be included in future climate change assessments.

## 1 Introduction

Dust aerosols are a key component of the Earth's system, which contribute to more than half of the total aerosol mass in the atmosphere (Kinne et al., 2006; Textor et al., 2006). They affect global climate directly by absorbing and scattering solar and terrestrial radiation and indirectly by serving as cloud condensation nuclei (CCN) and ice nucleating particles (INPs) to alter the cloud properties. They also have an impact on the surface concentration of particular matters, which consequently influences the air quality and human health (Chen et al., 2004). Additionally, dust aerosols play an important role in the biogeochemical cycle in that the contained metallic elements provide nutrients to ocean through deposition (Martin, 1990).

Dust is generally recognized as natural aerosol that is induced by wind erosion from arid and semi-arid regions – the global dust burden in the atmosphere is presumed to be stable with time. As a result, the Intergovernmental Panel on Climate Change (IPCC) Sixth Assessment Report (AR6) (Forster et al., 2021) does not account for dust when quantifying anthropogenic aerosol effective radiative forcing from pre-industrial (PI) to present day (PD). However, a recent work by Kok et al. (2023) reported a 55% ± 30% increase of atmospheric dust burden from PI to PD using a reconstruction dataset built upon dust historical deposition records, while the Coupled Model Intercomparison Project Phase 6 (CMIP6) models predict little historical trends for atmospheric dust loading. This suggests that current climate models have uncertainties in representing historical global dust emissions, and the climate assessment without considering dust historial changes is biased.

The substantial increase in the reconstructed dust loading can be at least partially attributed to the anthropogenic impacts on dust emissions (i.e., anthropogenic dust, AD). It has been noted for a long time that dust emissions are related to anthropogenic activities (Penner et al., 1994). However, there is no consensus on the definition of AD. Zender et al. (2004) classified the AD into two categories: (1) those related to anthropogenic land use change that changes soil surface conditions, and (2) those modified by anthropogenic climate changes, such as the changes in surface wind, soil moisture, and precipitation. The first kind of AD includes both direct mechanical injection of dust caused by anthropogenic activities (e.g., construction, transportation, and agricultural activities) (Chen et al., 2018) and AD due to wind erosion over the land surface disturbed by human activities (e.g., deforestation, overgrazing, overcultivation, inappropriate irrigation practices, and desiccation of rivers and lakes). Previous studies may only partially consider the above categories of AD.

Quantifying the contribution of AD to global dust cycle is highly uncertain. Modeling and observational estimates of the AD contribution spread in a wide range that goes from less than 10% to up to 60% (Chen et al., 2018; Ginoux et al., 2012; Huang et al., 2015; Mahowald et al., 2004; Mahowald & Luo, 2003; Sokolik & Toon, 1996; Stanelle et al., 2014; Tegen et al., 2004; Tegen & Fung, 1995). One challenge for these studies lies in the separation of AD from natural dust (ND). Land use datasets are sometimes used in aid of the separation. Early studies, like Sokolik and Toon (1996), simply assumed that the AD loading is linearly proportional to the land area converted to deserts by human activities. More recently, Ginoux et al. (2012) identified dust sources

using the Moderate-Resolution Imaging Spectroradiameter (MODIS) frequency-of-occurrence (FoO) distributions of dust optical depth (DOD) and then attributed AD and ND sources using the land use data from the History Database of the Global Environment (HYDE, Klein Goldewijk, 2001) – dust sources with land use exceeds 30% are AD sources; otherwise they are ND sources. The major AD sources identified in their study include the Sahel and the Mediterranean coast in North Africa, the north China plains and Saudi Arabia in Asia, as well as the high plains in North America. They further estimated the AD emission through applying the source function map derived from the MODIS FoO data to a global atmospheric model, which showed that the AD emissions account for 25% of global dust emissions. Moreover, Huang et al. (2015) combined the Cloud-Aerosol Lidar and Infrared Pathfinder Satellite Observation (CALIPSO) dust and planetary boundary layer (PBL) retrievals with the MODIS global land cover type product. By assuming that AD originates from different land cover from ND and is mostly trapped within PBL, they suggest that AD contributes to around 25% of global continental dust burden, which is in good agreement with the estimate by Ginoux et al. (2012). In addition, instead of using observational datasets, Stanelle et al. (2014) represented anthropogenic sources of dust through the simulated vegetation cover on each plant function type (PFT) in the land component of a global model. They found that 10% of dust particles in present day are emitted from anthropogenic (agricultural) sources.

For modeling studies, another open question is how to parameterize AD emission fluxes. Currently, AD emissions are generally simulated by modifying the ND emission

parameterizations for identified AD sources. The threshold of wind friction velocity is a parameter commonly tuned for AD emissions. Both Stanelle et al. (2014) and Ginoux et al. (2012) increased the threshold velocity to account for the soil conservation practices which are employed to reduce the wind erosion. However, other studies decreased this threshold velocity by assuming that the soil disturbed by anthropogenic activities is more vulnerable to wind erosion (Chen et al., 2018; Tegen et al., 2004). The above inconsistency indicates that large uncertainty exsits in the understanding of AD emissions.

The Energy Exascale Earth System Model version 1 (E3SMv1) is a global Earth system model developed by the U.S. Department of Energy (Golaz et al., 2019). The baseline E3SMv1 does not account for AD emission and predicts a small decreasing trend in dust burden after 1950 (Zhang et al., 2022), which, like many other CMIP6 models, is not consistent with the increasing trend of dust burden as shown in Kok et al. (2023). In this study, we develop a new method to parameterize the AD emission and implement it in E3SMv1. The parameterization uses the fraction of crop PFT from the land component of E3SMv1. The paper is organized as follows. Section 2 introduces the E3SMv1 model, our new AD parameterization, and the model experiment setup. Section 3 provides a description of the observational data we use. Section 4 evaluates the new parameterization against observations, investigates the historical change of AD emission from PI to PD, and quantifies the direct effective radiative forcing of AD. Finally, we discuss the uncertainties of our study in Section 5 and summarize the results in Section 6.

# 2 Model

## 2.1 E3SM model

We use the atmosphere and land components of E3SMv1 (J. Golaz et al., 2019; Rasch et al., 2019) in this study. E3SM Atmosphere Model version 1 (EAMv1) includes parameterizations for deep convection (Zhang & McFarlane, 1995), cloud microphysics (Gettelman & Morrison, 2015), as well as a unified parameterization for cloud macrophysics, turbulence, and shallow convection following Cloud Layers Unified by Binormals (CLUBB; Bogenschutz et al., 2013; Golaz et al., 2002; Larson & Golaz, 2005). Atmospheric aerosols are treated through a four-mode version of modal aerosol module (MAM4) (Liu et al., 2016; Wang et al., 2020), which predicts the number and mass mixing ratios of seven aerosol species (i.e., dust, black carbon, primary organic aerosol, secondary organic aerosol, sulfate, sea salt, and marine organic aerosol) in four lognormal size modes (Aitken, accumulation, primary carbon, and coarse modes). Dust aerosols are carried in the accumulation and coarse modes. The aerosol optical properties are parameterized following Ghan and Zaveri (2007), while the dust optical properties are updated according to Albani et al. (2014). We note that MAM4 neglects the longwave scattering of dust aerosols and only accounts for the longwave absorption as well as the shortwave absorption and scattering. Dust aerosols in the model also interact with cloud formation through acting as CCN in liquid clouds (Abdul-Razzak & Ghan, 2000) and INPs in stratiform mixed-phase clouds (Wang et al., 2014) and cirrus clouds (Liu et al., 2007; Liu & Penner, 2005). The wet (in-cloud nucleation and below-cloud

scavenging) and dry deposition of dust are treated together with the other aerosol species in the same aerosol mode.

The land component in E3SMv1 is the E3SM land model version 0 (ELMv0). It is modified from the Community Land Model version 4.5 (CLM4.5) (Oleson et al., 2013). To represent the spatial land surface heterogeneity, each grid cell in ELMv0 is composed of multiple land units. Each land unit can be further divided into several columns, such as snow/soil columns. The soil column is composed of up to 15 PFTs (including 8 types of trees, 3 types of shrubs, 3 types of grass, and one type of crop) plus bare ground. The vegetation coverage over each PFT is defined by leaf and steam area indices. The seasonal vegetation changes are based on satellite phenology, which is a climatology of satellite remote sensing data (Lawrence & Chase, 2007).

## 2.2 Dust emission parameterization in E3SMv1

The dust emission flux is parameterized in ELMv0 following Zender et al. (2003; hereafter Z03). The total vertical dust emission flux, $F_d$, is given by

$$F_d = TS_{geo} f_m \alpha Q_s, \quad (1)$$

where $T$ is a global uniformed tuning factor; $S_{geo}$ is the geomorphic soil erodibility; $f_m$ is the grid cell fraction of exposed bare soil; $\alpha$ is the sandblasting mass efficiency; and $Q_s$ is the total horizontally saltating mass flux. $S_{geo}$ is a measure of the soil's ability to produce dust emission for a given meteorological forcing, which is proportional to the upstream runoff collection area (Zender & Newman, 2003). The factor $f_m$ is given by

$$f_m = (1 - f_{lake} - f_{wetl})(1 - f_{sno})(1 - f_v)\frac{w_{liq,l}}{w_{liq,l}+w_{ice,l}}, \quad (2)$$

where $f_{lake}$, $f_{wetl}$, and $f_{snow}$ are the ELMv1's grid cell fractions of lake, wetland, and snow cover, respectively; $w_{liq,l}$ and $w_{ice,l}$ are the topsoil layer liquid water and ice water contents, respectively. $f_v$ is the vegetation cover fraction that is assumed to increase linearly with the leaf and stem area index (LAI), $\lambda$, and given by

$$f_v = \lambda/\lambda_{thr}, (\lambda \leq \lambda_{thr}). \quad (3)$$

Here, $\lambda_{thr} = 0.3$ m$^2$ m$^{-2}$ is the threshold of LAI above which no dust emission is allowed (Mahowald et al., 2006). The LAI is averaged over all the PFTs.

The horizontally saltating flux, $Q_s$, is given by

$$Q_s = \frac{c_s \rho_{atm} u_{*s}^3}{g}(1 - \frac{u_{*t}}{u_{*s}})(1 + \frac{u_{*t}}{u_{*s}})^2, (u_{*s} > u_{*t}), \quad (4)$$

where $c_s = 2.61$; $\rho_{atm}$ is the surface air density, $g$ is the gravitational acceleration constant; $u_{*s}$ is the wind friction speed; and $u_{*t}$ is the threshold wind friction speed for saltation. $u_{*t}$ is proportional to $f_w$, which is a factor depending on soil moisture and is given by

$$f_w = 1, (w \leq w_t), \quad (5)$$

$$f_w = \sqrt{1 + 1.21[100(w - w_t)]^{0.68}}, (w > w_t). \quad (6)$$

$w$ and $w_t$ are gravimetric water content of the top soil layer and its threshold, respectively. According to Fecan et al. (1999), $w_t$ is a function of soil's clay fraction ($M_{clay}$, ranging from 0 to 1):

$$w_t = a(0.17M_{clay} + 0.14{M_{clay}}^2), \quad (7)$$

where $a$ is a tuning parameter and is set to $1/M_{clay}$ by Z03. A smaller value of $a$ indicates a larger effect of soil moisture on $u_{*t}$.

212 According to the dust emission size distribution in Z03, 3.2% and 96.8% of the
213 total dust emission mass flux are distributed into the accumulation and the coarse aerosol
214 modes, respectively, in EAMv1. This is the default setting of the model. We note this
215 size distribution leads to an overestimation of dust emission in clay size (< 2 μm
216 diameter) (Kok, 2011; Kok et al., 2017).

217 **2.3 Parameterization for AD emissions**

218 By default, Z03 parameterization only includes ND emissions. In this study, we
219 apply a modified Z03 parameterization to the AD sources to represent AD emissions.
220 The fraction of potential AD sources in each grid cell is defined as the exposed bare soil
221 fraction of crop PFT ($f_{m,ant}$) in an ELMv0 grid cell. $f_{m,ant}$ is determined following Eq.
222 (2) but only the LAI for the crop PFT is used to calculate the vegetation cover fraction
223 ($f_v$, see Eq. (3)). This method is similar to Stanelle et al. (2014), where they identified
224 the AD sources using LAI on each PFT in the land component of the ECHAM6 model.
225 Two other major modifications are made to the Z03 parameterization when
226 applied to the AD sources. First, to increase the impact of soil moisture, the tuning factor
227 $a$ in Eq. (7) is reduced from $1/M_{clay}$ to 1 when calculating the soil water content
228 threshold ($w_t$). This modification results in an increase of the threshold wind friction
229 speed ($u_{*t}$) used in the calculation of the saltating flux for AD ($Q_{s,ant}$), which is
230 consistent with Stanelle et al. (2014) and Ginoux et al. (2012). Second, the AD emission
231 is set to zero when soil moisture content is larger than 25% to prevent unrealistic
232 emissions from Europe (not shown). With the two modifications above, we allow for the

stronger suppression of soil moisture on dust emission than the default parameterization, which can better simulate dust emissions over cropland.

With all these modifications, Eq. (1) is revised to

$$F_d = TS_{geo} f_{m,ND} \alpha Q_s + T_{AD} S_{AD} f_{m,AD} \alpha Q_{s,AD}, \quad (8)$$

where the first and the second terms on the righthand side represent emission fluxes for ND and AD, respectively. The ND emission flux is slightly modified compared to Eq. (1), because the LAI over crop PFT is not included in the calculation of $f_{m,ND}$ to avoid double counting. $T_{AD}$ is the tuning factor for AD. $S_{AD}$ is the source function for AD, which is currently set to 1 globally. In summary, we define AD emissions as agricultural dust emissions from crop PFT, while dust emissions from the other PFTs are considered as ND emissions.

Moreover, to explicitly track natural and anthropogenic dust emissions, we implement the dust source tagging technique (Shi et al., 2022) in EAMv1 by adding AD to a separate tracer from ND. With the tagging technique, anthropogenic and natural dust undergo the abovementioned processes independently from each other.

Similar to Stanelle et al. (2014), our modifications physically link the AD emission to the change of land type and vegetation coverage in the land component of E3SMv1. By avoiding using an empirical soil source function map that is based on present-day observations, our approach has the flexibility to simulate AD emissions in the past and future climate.

### 2.4 Experiment setup

The experiments we conducted for this study are summerized in Table 1. To evaluate the performance of our new parameterization, a control experiment based on the standard E3SMv1 model (labeled as CTRL) and an experiment including our modifications regarding AD emission and dust tagging (labeled as NEW) were performed. For the two experiments, the E3SMv1 model was integrated from January 2000 to December 2010 at 1° horizontal resolution with 72 vertical layers. The first-year results were treated as spin-up and the last ten years (from 2001 to 2010) were used in our analysis. The sea surface temperature (SST) is prescribed using the climatology from 1870 to 2009. The horizontal wind components were nudged to the Modern-Era Retrospective Analysis for Research and Applications version 2 (MERRA-2) reanalysis data (Gelaro et al., 2017) with a relaxation time scale of 6 h using the linear function nudging strategy as described in Sun et al. (2019). The land surface data (including land fraction for crop PFT) follows the year 2000 to represent the AD emission in PD conditions. The emission for anthropogenic and biomass burning aerosols as well as the concentrations of tracer gases (e.g., the greenhouse gases) are prescribed using the data of 2000. We note that the MERRA-2, SST, emission, and land use data used for the simulations are from different years due to the availiability of the datasets, which may results in inconsistency. It is also noted that the global dust emission in CTRL and NEW were tuned so that the global total dust emission in the two experiments are close to each other and the global averaged DOD is within the range of observational estimates (0.030±0.005) by Ridley et al. (2016) (See details below in Section 4.1).

Moreover, we conducted another experiments (labeled as NEW_PI) to estimate the effective radiative forcing of dust due to aerosol-radiation interactions ($ERF_{ari}$) from PI to PD. The setup for the experiment is the same as NEW, except that it uses the land surface data for 1850 to represent the dust emissions in the PI condition. The $ERF_{ari}$ of dust is calculated following Ghan (2013)'s method with the equation below:

$$ERF_{ari} = \Delta(F - F_{clean}). \quad (9)$$

Here, Δ represents the difference between the experiments with dust emissions in PD and PI conditions (i.e., NEW minus NEW_PI). $F$ are the all-sky radiative fluxes, while $F_{clean}$ are the radiative fluxes under no aerosol conditions. A caveat of this method is that different land cover datasets used in NEW and NEW_PI may impact the estimated $ERF_{ari}$ through changes in surface albedo. Details regarding $ERF_{ari}$ are provided in Section 4.3. In addition, we note the effective radiative forcing of dust due to aerosol-cloud interactions ($ERF_{aci}$) is not estimated in this study because the surface albedo differences between PI and PD largely impact the estimate of $ERF_{aci}$.

## 3 Observations

### 3.1 MIDAS

The ModIs Dust AeroSol (MIDAS) dataset (Gkikas et al., 2021) provides daily DOD at 550nm at ~ 0.1° horizontal resolution on a global scale. This dataset derives DOD by combining aerosol optical depth (AOD) from MODIS-Aqua (Collection 6.1; Level 2) with DOD-to-AOD ratios from MERRA-2 reanalysis data. In our study, we use

the data from 2003 to 2010 and process the original data to an annual mean DOD at 1° horizontal resolution. The processed MIDAS DOD is compared with annual mean simulated DOD from 2001 to 2010.

### 3.2 Dust deposition flux measurements

The dust deposition flux dataset, which consists of 84 stations, was compiled by Huneeus et al. (2011). This compilation includes measurements from Ginoux et al. (2001), Mahowald et al. (2009), Mahowald et al. (1999), and the Dust Indicators and Records in Terrestrial and Marine Paleoenvironments database (Kohfeld & Harrison, 2001; Tegen et al., 2002). In general, the observation sites are located at relatively remote regions. It is noted that the measurements were collected during the late $20^{th}$ centuries, while we compare them against modelling results over the period 2001-2010 to evaluate the model from a climatological perspective. Systematic errors are introduced here because the period of the simulation does not coincident with that of the measurements. Moreover, we use simulated dust over the whole size range (< 10 μm) for the comparison whereas the size range of the measurements is unknown, which is likely to be another source of uncertainties in the comparison. Also, comparing model results at ~100 km resolution with deposition flux data measured at stations leads to representative biases (same source of bias also exists for the ground-based measurements introduced in Sections 3.3 and 3.4 below).

### 3.3 AERONET AOD

The Aerosol Robotic NETwrok (AERONET) (Holben et al., 1998) conducts sun photometer sky radiance measurements that are inverted to produce aerosol properties across the world. Following Kok et al. (2014), we process the level 2.0 quality assured AOD from version 2 direct sun algorithm during the simulation time period (2001 to 2010) at 40 "dust-dominated" sites, which include 16 in North Africa, 11 in Middle East, 6 in rest of Asia, 3 in Australia, and 4 in Atlantic. Most of the sites locate at regions close to the AD sources identified by Ginoux et al. (2012). It is noted that the AERONET AOD measurements are biased towards clear-sky conditions due to the cloud-screening procedure (Smirnov et al., 2000).

### 3.4 IMPROVE dust and aerosol concentrations measurements

The Interagency Monitoring of Protected Visual Environments (IMPROVE; Malm et al., 1994) network operates filter based surface aerosol measurements across the United States. Here, we use the fine dust (FD) and coarse aerosol mass (CM) concentrations from the IMPROVE network during the simulation period (2001 to 2010). The observed FD concentrations are estimated from an empirical relationship with the isotopic mass concentrations of aluminium, silicon, calcium, iron, and titanium (Malm et al., 1994). They only include dust particles with diameter smaller 2.5 μm and are compared with simulated dust concentrations at the same size range. The CM concentrations are determined by the difference of the measured PM10 and PM2.5 mass. They are compared with simulated total aerosol mass in the same size range. Previous

335 studies use CM as a proxy for dust (e.g., Wu et al., 2018). A CM speciation study at 9
336 IMPROVE sites that represent the continental US found that crustal minerals (i.e., dust)
337 accounts for 34% to 76% of the CM concentrations, which makes dust the single largest
338 contributor to CM in all the stations except the Mount Rainier site (Malm et al., 2007).
339 However, other aerosols, like carbonaceous aerosols, nitrate, and sulfate, may also
340 contribute to CM. Therefore, to further eliminate the contribution from non-dust aerosols,
341 we select the CM data only when the simulated dust accounts for more than 90% of the
342 total aerosol mass for the comparisons. The location of the IMPROVE sites are shown in
343 Figure S1. In total, we select 194 and 67 stations for FD and CM comparisons,
344 respectively.

345 **4 Results**

346 **4.1 Present-day dust emission and global dust cycle**

347 Figure 1 shows the simulated dust emission fluxes from the NEW and CTRL
348 experiments at PD. The global total dust emission flux from NEW is 4263 Tg $yr^{-1}$, with
349 ND and AD accounting for 3695 Tg $yr^{-1}$ and 567 Tg $yr^{-1}$, respectively. The AD emission
350 contributes 13.3% to the total dust emission, which is lower than the estimate (25%) by
351 Ginoux et al. (2012) but comparable with the estimate (10%) from Stanelle et al. (2014).
352 The AD emission sources in NEW locate in the Great Plains of the North America, the
353 Sahel and the Atlas Mountains of North Africa, East European Plain and Central Asia,
354 highlands of Saudi Arabia in the Middle East, Pakistan and North India in South Asia,

North and Northeast China plains in East Asia, and the southwest of Australia (Figure 1d). These AD sources are corroborated with the sources identified by Ginoux et al. (2012) using the MODIS data, except those located in East Europe and northern part of Central Asia. One possible reason for this is that the MODIS data they utilized only extends to 50°N and does not include East Europe and northern part of Central Asia. We note that previous observational studies (e.g., Verheijen et al., 2009) have reported agriculatural dust emissions over East Europe, which supports our results. The Central Asia AD emissions were also identified by Stanelle et al. (2014) that agrees with our results. Overall, the global spatial distribution of the simulated AD emissions is largely correlated with the crop PFT fraction (Figure 1e) but also related to the vegetation coverage, soil moisture, and surface wind speed. The total emission flux from NEW (4263 Tg $yr^{-1}$) is comparable with that from CTRL (4106 Tg $yr^{-1}$) due to the model tuning of global DOD mentioned in Section 2.4, while the dust sources simulated by CTRL are mostly classified as the ND ones in NEW. This indicates that the dust emissions are redistributed in NEW by lowering the ND emissions and representing the AD sources compared to CTRL.

Table 2 summarizes the global dust budget of CTRL and NEW experiments, while the spatial distributions of dust optical depth (DOD) are shown in Figure 2. The global and annual mean DOD from the NEW experiment is 0.028, which is within the observational estimate (0.030±0.005) by Ridley et al. (2016). The global distribution of AD DOD correlates with the AD emissions (Figure 1d), with the maximum values in East Sahel, the Atlas Mountain, North India, and North China. The global and annual

mean DOD from NEW is close to that from CTRL (0.029) because of the tuning strategy applied to the global total dust emission. However, the spatial distributions of total DOD are slightly different in the two experiments (Figure 2e) – the NEW experiment simulates larger DOD at regions close to AD sources but smaller DOD over major ND sources (e.g., Sahara and Gobi Desert), which is consistent with the aforementioned redistribution of dust emission in NEW. The total dust burden in NEW is 22.0 Tg, which is within the range of the AeroCom (Aerosol Comparisons between Observations and Models) models (8 to 30 Tg; Huneeus et al., 2011). The total dust burden from NEW is also close to that from CTRL. The contributions of AD to total DOD and total dust burden in NEW are 10.7% and 10.9%, respectively, which are slightly smaller than the contribution (13.3%) of AD to total dust emission because of the shorter lifetime of AD (1.52 days) than that of ND (1.94 days). This indicates a faster removal of AD than ND from the atmosphere, likely associated with the fact that AD is emitted from cropland and trapped within PBL whereas ND from deserts can be uplifted above PBL (e.g., by cold fronts) during emissions and undergo the long-range transport (Huang et al., 2015). We note that the dry removal rate (i.e., dry deposition flux devided by burden) for AD (188 $yr^{-1}$) is much larger than that for ND (147 $yr^{-1}$), which indicates a stronger dry deposition of AD that is corroborated with its possibly weaker vertical transport. The lifetime of total dust from NEW (1.88 days) is slightly shorter than that from CTRL (1.94 days), while the lifetime of ND from NEW (1.94 days) is the same as that from CTRL.

398 **4.2 Model evaluation**

399 The comparisons between simulated DOD and the MIDAS dataset are shown in
400 Figure 3. Overall, NEW and CTRL perform similarly when comparing with MIDAS.
401 The misrepresentations of simulated DOD are mainly caused by biases in the ND
402 emissions and atmospheric processes that affect dust transport and deposition. For
403 example, both CTRL and NEW show underestimations over West Sahara and
404 overestimations over East Sahara, which are known biases related to the geomorphic
405 source function used by the Z03 dust emission parameterization (Wu et al., 2020).
406 However, regional changes related to the AD emissions are also presented. The CTRL
407 experiment has stong low biases over North India, which is turned into high biases after
408 including the AD emissions in NEW (Figure 1d). The newly represented AD sources in
409 North China also result in an overprediction in NEW, which is not shown in CTRL. The
410 AD emissions also lead to a larger DOD in NEW than CTRL over the Bay of Bengal,
411 Southeast Asia, and South China (Figure 2e), which reduces the low biases over these
412 regions or even turn them into high biases in NEW. In addition, the underprediction over
413 the central US in CTRL is slightly improved in NEW, since the NEW experiment
414 predicts larger DOD over there due to the local AD emissions (Figure 2e).

415 The NEW and CTRL experiments also perform similarly well in the comparison
416 with the global dust deposition flux dataset (Figure 4) – both experiments show
417 reasonably good agreement with observations with a correlation coefficient (R) of 0.86.
418 One major reason for the similar performance is that most of the deposition
419 measurements were conducted at remote regions. Since the AD sources are generally

close to the ND sources, the impact of different source locations is minimalized when dust aerosols reach remote regions after the long-range transport.

The impact of newly added AD emissions becomes more noticable when moving to the regions close to dust sources. Figure 5 shows the simulated AOD in CTRL and NEW experiments compared with the AERONET AOD at these stations. The comparison of the AOD seasonal cycle at each station is shown in Figure S2. We note that many of these stations are significantly influenced by ND because they are located close to the major ND sources. Despite of this, including AD sources in NEW still obviously improves the agreement with observations as compared to CTRL – the overall correlation of the comparison increases from 0.85 in CTRL to 0.90 in NEW, while the magnitude of the mean bias (MB) reduces by half in NEW. The most significant improvement occurs in Asia, where the underestimation of AOD is reduced by nearly 10 times (from -0.109 to -0.011). This is mainly due to the newly simulated AD sources in North India that turn the underestimation at Kanpur and Jaipur stations into slight overestimation (panel a3 and a4 in Figure S2). This change is consistent with the MIDAS comparison in North India (Figure 3). These two stations show large high biases during late spring and early summer in the NEW experiment, which possibly indicates a wrong seasonal cycle of AD emissions in North India. In addition, the underprediction of the AOD in North Africa is also slightly improved in NEW. We notice that the simulated AD DOD in NEW tends to peak between Janauray and April over the Sahel regions (panel c1, c5, c7-c11, c14, and c16 in Figure S2), which may be linked to the low LAI over cropland during this time. As a result, the NEW experiment shows improvement

during early spring at several stations in Sahel, like Ouagadougou, Ilorin, and Djougou (panel c5, c7, and c10 in Figure S2, respectively).

Figure 6 shows the comparison of simulated surface FD and CM concentrations with measurements from the US IMPROVE network. Since the network stations are mostly in considerable distances from the major ND sources, the impacts of AD emissions are profound. Including AD in the NEW experiment results in an overprediction of simulated FD (MB changes from -0.10 $\mu g\ m^{-3}$ in CTRL to 0.40 $\mu g\ m^{-3}$ in NEW), which makes the comparisons between model and observation worse (R decreases from 0.685 to 0.520). The high biases in NEW mainly occur at regions close to AD sources that have relatively high FD concentrations, whereas the NEW experiment outperforms the CTRL experiment at relatively remote regions where the simulated FD concentrations is less than 0.3 $\mu g\ m^{-3}$. In contrast, the NEW experiment shows obvious improvements in simulating CM concentrations, which is evident by an increase in R from 0.36 to 0.48 and a reduction in the magnitude of MB from -3.23 $\mu g\ m^{-3}$ to -0.44 $\mu g\ m^{-3}$ as compared to the CTRL experiment. The inconsistency in the comparisons of FD and CM concentrations may be due to the overestimation of dust emissions in clay size (Kok, 2011) in E3SMv1.

Overall, the above evaluations validate our new parameterization's ability to (1) simulate global dust cycle comparably well as the baseline model and (2) capture the AD sources reasonably well as indicated by obvious regional improvements. Next we will use our AD parameterization to futher examine the climate impacts of AD.

### 4.3 Historical change of dust and the $ERF_{ari}$

In this section, we examine the historical change of dust emission and the consequent dust $ERF_{ari}$ due to the land cover change from PI to PD. The dust emissions under PI and PD land cover are simulated from NEW_PI and NEW experiments, respectively. The dust budget from NEW_PI is shown in Table 2, while Figure 7a and 7b shows the global distributions of ND and AD emissions in the PI land cover condition. The total dust emission increases by 495 Tg $yr^{-1}$ (13.1%) from PI to PD, accompanied by a 11.7% increase in the global total dust burden. We note this increase is smaller than the estimate (24.5%) by Stanelle et al. (2014), because they considered the impact of climate change other than that the impact of land use change. The increase in dust emission is dominated by a 347 Tg $yr^{-1}$ increase in the AD emission – specifically, the AD emission increases by 158% from 220 Tg $yr^{-1}$ to 567 Tg $yr^{-1}$ from PI to PD. The AD emission increases over all the AD sources globally from PI to PD (Figure 7d), due to the agricultural expansion that is reflected by the increase of cropland fraction (Figure 7e and Figure 1e). The ND emission also slightly increases (by less than 5%) from PI to PD (Figure 7c). One possible reason is that the increase in cropland consumes forest and grassland, which reduces the grid-mean LAI and thus exposed more bare soil as potential ND sources (i.e., $f_{m,ND}$ increases in Eq. (8) because LAI decreases in Eq. (3)). The meteorology changes (e.g., winds and precipitation) due to land use change may also contribute to the regional changes in the ND emission. Overall, the impact of land use change on ND is much smaller than that on AD. However, it is worth noting that

484 same soil erodibility map is used in the ND emission parameterization for the PI and PD
485 conditions, which may reduce the sensitivity of ND emissions to the land use change.
486 Finally, we quantify the all-sky TOA $ERF_{ari}$ of dust due to the land cover change
487 from PI to PD (Figure 8). The increase in total dust emission induces a negative
488 shorwave $ERF_{ari}$ of -0.05 W $m^{-2}$ and a positive longwave $ERF_{ari}$ of 0.009 W $m^{-2}$ (Figure
489 8a-b), which are due to more scattering of solar radiation and more absorbption of
490 longwave radiation by dust in PD than PI, respectively. The statistically significant
491 $ERF_{ari}$ of dust are mostly found near the AD sources, indicating a dominant contribution
492 of AD. We also note that the moderately positive shortwave $ERF_{ari}$ (Figue 8a) over the
493 mid-latitude regions in North America and Eurasia is likely related to suface albedo
494 change because of the deforestation in PD, instead of changes in dust. The resulting net
495 $ERF_{ari}$ of dust is -0.041 W $m^{-2}$ from PI (1850) to PD (2000) (Figure 8c). This is
496 substaintial compared to the IPCC AR6 estimate of total aerosol $ERF_{ari}$ (-0.3 ± 0.3 W $m^{-2}$)
497 from 1750 to 2014, which highlights the important role of dust from anthropogenic
498 land cover change in the regional and global climate changes.
499 In addition, we estimate the clear-sky TOA $ERF_{ari}$ of dust as shown in Figure S3,
500 which are -0.071, 0.011, and -0.06 W $m^{-2}$ for shortwave, longwave, and net radiation,
501 respectively. Our estimate is in good agreement with the clear-sky dust $ERF_{ari}$ (-0.05 W
502 $m^{-2}$) due to anthropogenic land cover change from Stanelle et al. (2014).

## 5. Discussion

In this study, we predict a 11.7% increase in global dust burden due to the land cover change from PI to PD (Table 2). This increase is higher than most of the CMIP6 models included in the study by Kok et al. (2023), whereas it is still smaller than the increase (55 ± 30%) shown by the reconstruction data. Below we provide several possible explanations.

The AD emission parameterization developed in our study only accounts for the AD produced from wind erosion over the cropland. The wind erosion from other land types, like pastureland, and direct AD emission due to anthropogenic activities (e.g., construction, traffic, and agricultural practices with heavy equipments) are not included. This indicates that the AD emission in the PD condition may be underestimated. Since anthropogenic activities and land use changes are more intense in PD than PI, it is likely that our estimate of the historical dust emission increase is also underpredicted. Moreover, we only examine the effect of land use changes on dust emissions, while the climate change factors (e.g., changes in surface wind and soil moisture due to anthropogenic climate change) are ignored. Stenelle et al. (2014) noted that anthropogenic climate change is almost equally important in the increase of historical dust emission as compared to the anthropogenic land use change. A regional study also found that climatic factors are the main driver of recent decline of dust activity in East Asia, while vegetation cover change due to land use managements plays only a minor role (Wu et al., 2022). This indicates that the dust change from PI to PD estimated in our study may be biased low without considering the impact of climate change. If the above

525 uncertainties are well addressed, the increase of dust emission from PI to PD may be
526 enlarged, which better matches the estimate by Kok et al. (2023). In this case, the
527 magnitude of $ERF_{ari}$ of dust is likely to increase, which emphasizes the important
528 contribution of dust to total anthropogenic aerosol radiative forcing.

529 Moreover, this study focuses on the direct radiative forcing of AD, while its
530 indirect forcing is also of great interest. Dust aerosols are efficient INPs that can
531 influence the phase partition of mixed-phase clouds (Shi & Liu, 2019), which have
532 important implications on climate feedback (Murray et al., 2021). In particular,
533 agriculatural dust was found to have distinct ice nucleating ability compared with
534 mineral dust from desert (ND) at warm temperatures (Steinke et al., 2016), which
535 indicates that AD and ND may have different impacts on low-level mixed-phase clouds.
536 Future studies are needed to investigate these topics.

537 In addition, our AD parameterization is simplified, because it only relates the AD
538 emissions to crop land use. In reality, other factors, like types of crops and agricultural
539 practices, may also have an impact of AD emission. In our future work, we will
540 incorporate our AD parameterization with an interactive crop model to take into account
541 these aspects more comprehensively.

542 Finally, in addition to their climate impacts, dust aerosols may substantially
543 influence the air quality and human health. The 1930s Dust Bowl in the Southern Great
544 Plains of North America, which is partially due to poor agricultural practices, resulted in
545 increasing death and illness from acute respiratory infections (Worster, 2004). Moreover,
546 a recent study finds that anthropogenic dust from urbanization worsens non-dust air

547 pollution through inducing surface radiative cooling that reduces the planetary boundary
548 layer height in urban regions (Xia et al., 2022). A detailed analysis is needed to closely
549 evaluate the contribution of AD to human health effects, which is beyond the scope of
550 this paper. Here, we use population-weighted surface AD and ND concentrations in the
551 PM2.5 size range ($PWAD_{PM2.5}$ and $PWND_{PM2.5}$) as a simple metric to broadly
552 characterize their human-health-relevant impacts. As shown in Figure 9, the population
553 weighted surface concentrations have high values over the densely populated regions.
554 The contribution of $PWAD_{PM2.5}$ to total global mean population-weighted surface dust
555 concentration is 27.6%, which is more than twice of that before the population weighting
556 is applied. This indicates that the AD emission influences human health more efficiently
557 than the ND emission, mainly because the AD sources are located closer to human
558 habitation.

559 **6. Conclusions**

560 In this study, we developed a parameterization to account for the AD emissions
561 in E3SMv1, which physically links AD emissions to the crop PFT fraction used in the
562 land component of E3SMv1. According to our new parameterization, the global and
563 annual AD emission is 567 Tg $yr^{-1}$ in the PD condition, which contributes 13.3 % to the
564 total dust emission. The major AD sources locate at the Great Plains in the North
565 America, the Sahel and the Atlas Mountains in North Africa, East European Plain and
566 Central Asia, highlands of Saudi Arabia in Middle East, Pakistan and North India in
567 South Asia, North and Northeast China plains in East Asia, and the southwest of

Australia. The distribution of the AD sources from our parameterization generally agrees with the sources identified by Ginoux et al. (2012). The contribution of AD to the global DOD and dust burden are both about 11 %, which are slightly less than the AD contribution to the total dust emission, indicating a slightly shorter lifetime of AD than that of ND. We performed model evaluations against satellite retrievals and ground-based observations, which demonstrates the new parameterization's ability to represent AD emissions and global dust cycle reasonably well. We also found that AD can impact air quality and human health more efficiently than ND likely due to the proximity of AD sources to hunamn habitation.

We examined the historical change of dust emission from PI to PD. We found that total dust emission increases by 13.1 % from 1850 to 2000, which is dominated by the increase in AD emission due to the expansion of cropland from PI to PD. As a result, atmospheric dust burden increases by 11.7 %. Based on this, we estimated the all-sky TOA $ERF_{ari}$ of dust to be -0.041 W $m^{-2}$ from 1850 to 2000. This is more than 10 % of the total anthropogenic aerosol $ERF_{ari}$ (-0.3 ± 0.3 W $m^{-2}$) from 1750 to 2014 estimated by the IPCC AR6 report, which highlights the important role of dust in the regional and global climate change. Considering the anthropogenic land use change is predicted to continue in the future (Hurtt et al., 2020), more studies are needed to investigate the impact of dust as a forcing agent to the future climate.

**Acknowledgement**

This study was supported as part of the Enabling Aerosol-cloud interactions at GLobal convection-permitting scalES (EAGLES) project (project no. 74358), funded by the U.S. Department of Energy, Office of Science, Office of Biological and Environmental Research, Earth System Model Development (ESMD) program area. This research used resources of the National Energy Research Scientific Computing Center (NERSC), a U.S. Department of Energy Office of Science User Facility located at Lawrence Berkeley National Laboratory, operated under Contract No. DE-AC02-05CH11231 using NERSC awards ALCC-ERCAP0016315, BER-ERCAP0015329, BER-ERCAP0018473, and BER-ERCAP0020990. The Pacific Northwest National Laboratory is operated for the U.S. Department of Energy by Battelle Memorial Institute under contract DE-AC05-76RL01830. C. Wu is supported by the National Natural Science Foundation of China (grant 41975119).

**Availiability Statement**

MIDAS data is available at https://doi.org/10.5281/zenodo.4244106. AERONET data is available at https://aeronet.gsfc.nasa.gov/cgi-bin/draw_map_display_aod_v3?level=3. Data referred to Huneeus et al. (2011) can be downloaded from https://aerocom-classic.met.no/DATA/download/DUST_BENCHMARK_HUNEEUS2011/. IMPROVE data http://views.cira.colostate.edu/fed/Express/ImproveData.aspx. The E3SMv1 source code is available at https://github.com/E3SM-Project/E3SM.

607 **References**

608 Abdul-Razzak, H., & Ghan, S. J. (2000). A parameterization of aerosol activation 2.
609 Multiple aerosol types. *Journal of Geophysical Research: Atmospheres*, *105*,
610 6837–6844. https://doi.org/10.1029/1999JD901161

611 Albani, S., Mahowald, N. M., Perry, A. T., Scanza, R. A., Zender, C. S., Heavens, N. G.,
612 et al. (2014). Improved dust representation in the Community Atmosphere
613 Model. *Journal of Advances in Modeling Earth Systems*, *6*, 541–570.
614 https://doi.org/10.1002/2013MS000279

615 Bogenschutz, P. A., Gettelman, A., Morrison, H., Larson, V. E., Craig, C., & Schanen,
616 D. P. (2013). Higher-Order Turbulence Closure and Its Impact on Climate
617 Simulations in the Community Atmosphere Model. *Journal of Climate*, *26*,
618 9655–9676. https://doi.org/10.1175/JCLI-D-13-00075.1

619 Chen, S., Jiang, N., Huang, J., Xu, X., Zhang, H., Zang, Z., et al. (2018). Quantifying
620 contributions of natural and anthropogenic dust emission from different climatic
621 regions. *Atmospheric Environment*, *191*, 94–104.
622 https://doi.org/10.1016/j.atmosenv.2018.07.043

623 Chen, Y.-S., Sheen, P.-C., Chen, E.-R., Liu, Y.-K., Wu, T.-N., & Yang, C.-Y. (2004).
624 Effects of Asian dust storm events on daily mortality in Taipei, Taiwan.
625 *Environmental Research*, *95*, 151–155.
626 https://doi.org/10.1016/j.envres.2003.08.008

627 Fécan, F., Marticorena, B., & Bergametti, G. (1999). Parametrization of the increase of
628 the aeolian erosion threshold wind friction velocity due to soil moisture for arid

629 and semi-arid areas. *Annales Geophysicae*, *17*, 149–157.
630 https://doi.org/10.1007/s00585-999-0149-7
631 Forster, P., Storelvmo, T., Armour, K., Collins, W., Dufresne, J.-L., Frame, D., et al.
632 (2021): The Earth's Energy Budget, Climate Feedbacks, and Climate Sensitivity.
633 In V. P. Masson-Delmotte et al. (Eds.), Climate Change 2021: The Physical
634 Science Basis. Contribution of Working Group I to the Sixth Assessment Report
635 of the Intergovernmental Panel on Climate Change (pp. 923-1054). Cambridge,
636 United Kingdom and New York, NY, USA: Cambridge University Press.
637 https://doi.org/10.1017/9781009157896
638 Gelaro, R., McCarty, W., Suárez, M. J., Todling, R., Molod, A., Takacs, L., et al. (2017).
639 The Modern-Era Retrospective Analysis for Research and Applications, Version
640 2 (MERRA-2). *Journal of Climate*, *30*, 5419–5454. https://doi.org/10.1175/JCLI-
641 D-16-0758.1
642 Gettelman, A., & Morrison, H. (2015). Advanced Two-Moment Bulk Microphysics for
643 Global Models. Part I: Off-Line Tests and Comparison with Other Schemes.
644 *Journal of Climate*, *28*, 1268–1287. https://doi.org/10.1175/JCLI-D-14-00102.1
645 Ghan, S. J. (2013). Technical Note: Estimating aerosol effects on cloud radiative forcing.
646 *Atmospheric Chemistry and Physics*, *13*, 9971–9974. https://doi.org/10.5194/acp-
647 13-9971-2013
648 Ghan, Steven J., & Zaveri, R. A. (2007). Parameterization of optical properties for
649 hydrated internally mixed aerosol. *Journal of Geophysical Research:*
650 *Atmospheres*, *112,* D10201. https://doi.org/10.1029/2006JD007927

651 Ginoux, P., Chin, M., Tegen, I., Prospero, J. M., Holben, B., Dubovik, O., & Lin, S.-J.
652 (2001). Sources and distributions of dust aerosols simulated with the GOCART
653 model. *Journal of Geophysical Research: Atmospheres*, *106*, 20255–20273.
654 https://doi.org/10.1029/2000JD000053
655 Ginoux, P., Prospero, J. M., Gill, T. E., Hsu, N. C., & Zhao, M. (2012). Global-scale
656 attribution of anthropogenic and natural dust sources and their emission rates
657 based on MODIS Deep Blue aerosol products. *Reviews of Geophysics*, *50*,
658 2012RG000388. https://doi.org/10.1029/2012RG000388
659 Gkikas, A., Proestakis, E., Amiridis, V., Kazadzis, S., Di Tomaso, E., Tsekeri, A., et al.
660 (2021). ModIs Dust AeroSol (MIDAS): a global fine-resolution dust optical
661 depth data set. *Atmospheric Measurement Techniques*, *14*, 309–334.
662 https://doi.org/10.5194/amt-14-309-2021
663 Golaz, J.-C., Caldwell, P. M., Van Roekel, L. P., Petersen, M. R., Tang, Q., Wolfe, J. D.,
664 et al. (2019). The DOE E3SM Coupled Model Version 1: Overview and
665 Evaluation at Standard Resolution. *Journal of Advances in Modeling Earth*
666 *Systems*, *11*, 2089–2129. https://doi.org/10.1029/2018MS001603
667 Golaz, J.-C., Larson, V. E., & William R. Cotton. (2002). A PDF-Based Model for
668 Boundary Layer Clouds. Part I: Method and Model Description. *Journal of the*
669 *Atmospheric Science*, *59*, 3540-3551. https://doi.org/10.1175/1520-
670 0469(2002)059<3540:APBMFB>2.0.CO;2
671 Holben, B. N., Eck, T. F., Slutsker, I., Tanré, D., Buis, J. P., Setzer, A., et al. (1998).
672 AERONET—A Federated Instrument Network and Data Archive for Aerosol

673 Characterization. *Remote Sensing of Environment*, *66*, 1–16.
674 https://doi.org/10.1016/S0034-4257(98)00031-5
675 Huang, J. P., Liu, J. J., Chen, B., & Nasiri, S. L. (2015). Detection of anthropogenic dust
676 using CALIPSO lidar measurements. *Atmospheric Chemistry and Physics*, *15*,
677 11653–11665. https://doi.org/10.5194/acp-15-11653-2015
678 Huneeus, N., Schulz, M., Balkanski, Y., Griesfeller, J., Prospero, J., Kinne, S., et al.
679 (2011). Global dust model intercomparison in AeroCom phase I. *Atmospheric*
680 *Chemistry and Physics*, *11*, 7781–7816. https://doi.org/10.5194/acp-11-7781-
681 2011
682 Hurtt, G. C., Chini, L., Sahajpal, R., Frolking, S., Bodirsky, B. L., Calvin, K., et al.
683 (2020). Harmonization of global land use change and management for the period
684 850–2100 (LUH2) for CMIP6. *Geoscientific Model Development*, *13*, 5425–
685 5464. https://doi.org/10.5194/gmd-13-5425-2020
686 Kinne, S., Schulz, M., Textor, C., Guibert, S., Balkanski, Y., Bauer, S. E., et al. (2006).
687 An AeroCom initial assessment – optical properties in aerosol component
688 modules of global models. *Atmospheric Chemistry and Physics, 6,* 1815-1834,
689 https://doi.org/10.5194/acp-6-1815-2006
690 Klein Goldewijk, K. (2001). Estimating global land use change over the past 300 years:
691 The HYDE Database. *Global Biogeochemical Cycles*, *15*, 417–433.
692 https://doi.org/10.1029/1999GB001232

693 Kohfeld, K. E., & Harrison, S. P. (2001). DIRTMAP: the geological record of dust.
694 *Earth-Science Reviews*, *54*, 81–114. https://doi.org/10.1016/S0012-
695 8252(01)00042-3
696 Kok, J. F. (2011). A scaling theory for the size distribution of emitted dust aerosols
697 suggests climate models underestimate the size of the global dust cycle.
698 *Proceedings of the National Academy of Sciences*, *108*, 1016–1021.
699 https://doi.org/10.1073/pnas.1014798108
700 Kok, J. F., Albani, S., Mahowald, N. M., & Ward, D. S. (2014). An improved dust
701 emission model – Part 2: Evaluation in the Community Earth System Model,
702 with implications for the use of dust source functions. *Atmospheric Chemistry*
703 *and Physics*, *14*, 13043–13061. https://doi.org/10.5194/acp-14-13043-2014
704 Kok, J. F., Ridley, D. A., Zhou, Q., Miller, R. L., Zhao, C., Heald, C. L., et al. (2017).
705 Smaller desert dust cooling effect estimated from analysis of dust size and
706 abundance. *Nature Geoscience*, *10*, 274–278. https://doi.org/10.1038/ngeo2912
707 Kok, J. F., Storelvmo, T., Karydis, V. A., Adebiyi, A. A., Mahowald, N. M., Evan, A.
708 T., et al. (2023). Mineral dust aerosol impacts on global climate and climate
709 change. *Nature Reviews Earth & Environment*, *4*, 71–86.
710 https://doi.org/10.1038/s43017-022-00379-5
711 Larson, V. E., & Golaz, J.-C. (2005). Using Probability Density Functions to Derive
712 Consistent Closure Relationships among Higher-Order Moments. *Monthly*
713 *Weather Review*, *133*, 1023–1042. https://doi.org/10.1175/MWR2902.1

714 Lawrence, P. J., & Chase, T. N. (2007). Representing a new MODIS consistent land
715 surface in the Community Land Model (CLM 3.0). *Journal of Geophysical*
716 *Research: Biogeosciences*, *112*, G01023. https://doi.org/10.1029/2006JG000168
717 Liu, X., Ma, P.-L., Wang, H., Tilmes, S., Singh, B., Easter, R. C., et al. (2016).
718 Description and evaluation of a new four-mode version of the Modal Aerosol
719 Module (MAM4) within version 5.3 of the Community Atmosphere Model.
720 *Geoscientific Model Development*, *9*, 505–522. https://doi.org/10.5194/gmd-9-
721 505-2016
722 Liu, X., & Penner, J. E. (2005). Ice nucleation parameterization for global models.
723 *Meteorologische Zeitschrift, 14,* 499-514. https://doi.org/10.1127/0941-
724 2948/2005/0059
725 Liu, X., Penner, J. E., Ghan, S. J., & Wang, M. (2007). Inclusion of ice microphysics in
726 the NCAR Community Atmospheric Model Version 3 (CAM3). *Journal of*
727 *Climate*, *20*, 4526–4547. https://doi.org/10.1175/JCLI4264.1
728 Mahowald, N. M., Engelstaedter, S., Luo, C., Sealy, A., Artaxo, P., Benitez-Nelson, C.,
729 et al. (2009). Atmospheric iron deposition: global distribution, variability, and
730 human perturbations. *Annual Review of Marine Science*, *1*, 245–278.
731 https://doi.org/10.1146/annurev.marine.010908.163727
732 Mahowald, N., Kohfeld, K., Hansson, M., Balkanski, Y., Harrison, S. P., Prentice, I. C.,
733 et al. (1999). Dust sources and deposition during the last glacial maximum and
734 current climate: A comparison of model results with paleodata from ice cores and

735 marine sediments. *Journal of Geophysical Research: Atmospheres*, *104*, 15895–
736 15916. https://doi.org/10.1029/1999JD900084
737 Mahowald, N. M., & Luo, C. (2003). A less dusty future? *Geophysical Research Letters*,
738 *30*, 1903. https://doi.org/10.1029/2003GL017880
739 Mahowald, N. M., Rivera, G. D. R., & Luo, C. (2004). Comment on "Relative
740 importance of climate and land use in determining present and future global soil
741 dust emission" by I. Tegen et al. *Geophysical Research Letters*, *31*, L24105.
742 https://doi.org/10.1029/2004GL021272
743 Mahowald, N. M., Muhs, D. R., Levis, S., Rasch, P. J., Yoshioka, M., Zender, C. S., &
744 Luo, C. (2006). Change in atmospheric mineral aerosols in response to climate:
745 Last glacial period, preindustrial, modern, and doubled carbon dioxide climates.
746 *Journal of Geophysical Research: Atmospheres*, *111*(D10).
747 https://doi.org/10.1029/2005JD006653
748 Malm, W. C., Sisler, J. F., Huffman, D., Eldred, R. A., & Cahill, T. A. (1994). Spatial
749 and seasonal trends in particle concentration and optical extinction in the United
750 States. *Journal of Geophysical Research: Atmospheres*, *99*, 1347–1370.
751 https://doi.org/10.1029/93JD02916
752 Malm, W. C., Pitchford, M. L., McDade, C., & Ashbaugh, L. L. (2007). Coarse particle
753 speciation at selected locations in the rural continental United States.
754 *Atmospheric Environment*, *41*(10), 2225–2239.
755 https://doi.org/10.1016/j.atmosenv.2006.10.077

Martin, J. H. (1990). Glacial-interglacial CO2 change: The Iron Hypothesis. *Paleoceanography*, *5*, 1–13. https://doi.org/10.1029/PA005i001p00001

Murray, B. J., Carslaw, K. S., & Field, P. R. (2021). Opinion: Cloud-phase climate feedback and the importance of ice-nucleating particles. *Atmospheric Chemistry and Physics*, *21*, 665–679. https://doi.org/10.5194/acp-21-665-2021

Oleson, K. W., Lawrence, D. M., Bonan, G. B., Drewniak, B., Huang, M., Levis, S., et al. (2013). Technical Description of version 4.5 of the Community Land Model (CLM) (NCAR/TN-503+STR). Boulder, CO: National Center for Atmospheric Research Earth System Laboratory

Penner, J. E., Charlson, R. J., Hales, J. M., Laulainen, N. S., Novakov, T., Leifer, R., et al. (1994). Quantifying and Minimizing Uncertainty of Climate Forcing by Anthropogenic Aerosols. *Bulletin of the American Meteorological Society*, *75*, 375–400. https://doi.org/10.1175/15200477(1994)075<0375:QAMUOC>2.0.CO;2

Rasch, P. J., Xie, S., Ma, P. -L., Lin, W., Wang, H., Tang, Q., et al. (2019). An Overview of the Atmospheric Component of the Energy Exascale Earth System Model. *Journal of Advances in Modeling Earth Systems*, *11*, 2377–2411. https://doi.org/10.1029/2019MS001629

Ridley, D. A., Heald, C. L., Kok, J. F., & Zhao, C. (2016). An observationally constrained estimate of global dust aerosol optical depth. *Atmospheric Chemistry and Physics*, *16*, 15097–15117. https://doi.org/10.5194/acp-16-15097-2016

777 Shi, Y., & Liu, X. (2019). Dust Radiative Effects on Climate by Glaciating Mixed-Phase
778 Clouds. *Geophysical Research Letters*, *46*, 6128–6137.
779 https://doi.org/10.1029/2019GL082504
780 Shi, Y., Liu, X., Wu, M., Zhao, X., Ke, Z., & Brown, H. (2022). Relative importance of
781 high-latitude local and long-range-transported dust for Arctic ice-nucleating
782 particles and impacts on Arctic mixed-phase clouds. *Atmospheric Chemistry and*
783 *Physics*, *22*, 2909–2935. https://doi.org/10.5194/acp-22-2909-2022
784 Smirnov, A., Holben, B. N., Eck, T. F., Dubovik, O., & Slutsker, I. (2000). Cloud-
785 Screening and Quality Control Algorithms for the AERONET Database. *Remote*
786 *Sensing of Environment*, *73*, 337–349. https://doi.org/10.1016/S0034-
787 4257(00)00109-7
788 Sokolik, I. N., & Toon, O. B. (1996). Direct radiative forcing by anthropogenic airborne
789 mineral aerosols. *Nature*, *381*, 681–683. https://doi.org/10.1038/381681a0
790 Stanelle, T., Bey, I., Raddatz, T., Reick, C., & Tegen, I. (2014). Anthropogenically
791 induced changes in twentieth century mineral dust burden and the associated
792 impact on radiative forcing. *Journal of Geophysical Research: Atmospheres*,
793 *119*, 13526-13546. https://doi.org/10.1002/2014JD022062
794 Steinke, I., Funk, R., Busse, J., Iturri, A., Kirchen, S., Leue, M., et al. (2016). Ice
795 nucleation activity of agricultural soil dust aerosols from Mongolia, Argentina,
796 and Germany. *Journal of Geophysical Research: Atmospheres*, *121*, 13559-
797 13576. https://doi.org/10.1002/2016JD025160

798 Sun, J., Zhang, K., Wan, H., Ma, P., Tang, Q., & Zhang, S. (2019). Impact of Nudging
799 Strategy on the Climate Representativeness and Hindcast Skill of Constrained
800 EAMv1 Simulations. *Journal of Advances in Modeling Earth Systems*, *11*, 3911–
801 3933. https://doi.org/10.1029/2019MS001831
802 Tegen, I., Werner, M., Harrison, S. P., & Kohfeld, K. E. (2004). Relative importance of
803 climate and land use in determining present and future global soil dust emission.
804 *Geophysical Research Letters*, *31*, L05105.
805 https://doi.org/10.1029/2003GL019216
806 Tegen, I., & Fung, I. (1995). Contribution to the atmospheric mineral aerosol load from
807 land surface modification. *Journal of Geophysical Research: Atmospheres*, *100*,
808 18707–18726. https://doi.org/10.1029/95JD02051
809 Tegen, I., Harrison, S. P., Kohfeld, K., Prentice, I. C., Coe, M., & Heimann, M. (2002).
810 Impact of vegetation and preferential source areas on global dust aerosol: Results
811 from a model study. *Journal of Geophysical Research: Atmospheres*, *107*, 4576.
812 https://doi.org/10.1029/2001JD000963
813 Textor, C., Schulz, M., Guibert, S., Kinne, S., Balkanski, Y., Bauer, S., et al. (2006).
814 Analysis and quantification of the diversities of aerosol life cycles within
815 AeroCom. *Atmospheric Chemistry Physics*, *6*, 1777-1813.
816 https://doi.org/10.5194/acp-6-1777-2006
817 Verheijen, F. G. A., Jones, R. J. A., Rickson, R. J., & Smith, C. J. (2009). Tolerable
818 versus actual soil erosion rates in Europe. *Earth-Science Reviews*, *94*, 23–38.
819 https://doi.org/10.1016/j.earscirev.2009.02.003

820 Wang, H., Easter, R. C., Zhang, R., Ma, P., Singh, B., Zhang, K., et al. (2020). Aerosols
821 in the E3SM Version 1: New Developments and Their Impacts on Radiative
822 Forcing. *Journal of Advances in Modeling Earth Systems*, *12*, e2019MS001851.
823 https://doi.org/10.1029/2019MS001851
824 Wang, Y., Liu, X., Hoose, C., & Wang, B. (2014). Different contact angle distributions
825 for heterogeneous ice nucleation in the Community Atmospheric Model version
826 5. *Atmospheric Chemistry and Physics*, *14*, 10411–10430.
827 https://doi.org/10.5194/acp-14-10411-2014
828 Worster D. (2004). Dust Bowl. Oxford, UK: Oxford University Press.
829 Wu, C., Liu, X., Lin, Z., Rahimi-Esfarjani, S. R., & Lu, Z. (2018). Impacts of absorbing
830 aerosol deposition on snowpack and hydrologic cycle in the Rocky Mountain
831 region based on variable-resolution CESM (VR-CESM) simulations.
832 *Atmospheric Chemistry and Physics*, *18*, 511–533. https://doi.org/10.5194/acp-
833 18-511-2018
834 Wu, C., Lin, Z., Shao, Y., Liu, X., & Li, Y. (2022). Drivers of recent decline in dust
835 activity over East Asia. *Nature Communications*, *13*, 7105.
836 https://doi.org/10.1038/s41467-022-34823-3
837 Wu, M., Liu, X., Yu, H., Wang, H., Shi, Y., Yang, K., et al. (2020). Understanding
838 processes that control dust spatial distributions with global climate models and
839 satellite observations. *Atmospheric Chemistry and Physics*, *20*, 13835–13855.
840 https://doi.org/10.5194/acp-20-13835-2020

841 Xia, W., Wang, Y., Chen, S., Huang, J., Wang, B., Zhang, G. J., et al. (2022). Double
842 Trouble of Air Pollution by Anthropogenic Dust. *Environmental Science &*
843 *Technology*, *56*, 761–769. https://doi.org/10.1021/acs.est.1c04779
844 Zender, C. S., Miller, R. L., & Tegen, I. (2004). Quantifying mineral dust mass
845 budgets:Terminology, constraints, and current estimates. *Eos*, *85*, 509–512.
846 https://doi.org/10.1029/2004EO480002
847 Zender, Charles S., & Newman, D. (2003). Spatial heterogeneity in aeolian erodibility:
848 Uniform, topographic, geomorphic, and hydrologic hypotheses. *Journal of*
849 *Geophysical Research*, *108*, 4543. https://doi.org/10.1029/2002JD003039
850 Zender, Charles S., Bian, H., & Newman, D. (2003). Mineral Dust Entrainment and
851 Deposition (DEAD) model: Description and 1990s dust climatology. *Journal of*
852 *Geophysical Research*, *108*, 4416. https://doi.org/10.1029/2002JD002775
853 Zhang, G. J., & McFarlane, N. A. (1995). Sensitivity of climate simulations to the
854 parameterization of cumulus convection in the Canadian climate centre general
855 circulation model. *Atmosphere-Ocean*, *33*, 407–446.
856 https://doi.org/10.1080/07055900.1995.9649539
857 Zhang, K., Zhang, W., Wan, H., Rasch, P. J., Ghan, S. J., Easter, R. C., et al. (2022).
858 Effective radiative forcing of anthropogenic aerosols in E3SM version 1:
859 historical changes, causality, decomposition, and parameterization sensitivities.
860 *Atmospheric Chemistry and Physics*, *22*, 9129–9160. https://doi.org/10.5194/acp-
861 22-9129-2022
862

863 **Table 1. Experiments conducted in this study.**

| Experiment | Description |
|---|---|
| CTRL | Standard configuration of E3SMv1. |
| NEW | A simulation including our new parameterization for AD emissions and the dust tagging technique to track AD and ND emissions. |
| NEW_PI | Same as New, but use 1850 land surface dataset |

864
865

866 **Table 2. Global dust budget.**

| | CTRL | NEW | | | NEW_PI | | |
|---|---|---|---|---|---|---|---|
| | | Total | ND | AD | Total | ND | AD |
| Emission (Tg $yr^{-1}$) | 4106 | 4263 | 3695 | 567 | 3768 | 3548 | 220 |
| DOD | 0.029 | 0.028 | 0.025 | 0.003 | 0.025 | 0.024 | 0.001 |
| Burden (Tg) | 21.9 | 22.0 | 19.6 | 2.4 | 19.7 | 18.8 | 0.8 |
| Lifetime (day) | 1.94 | 1.88 | 1.94 | 1.52 | 1.91 | 1.94 | 1.40 |
| Dry deposition (Tg $yr^{-1}$) | 3183 | 3336 | 2884 | 452 | 2945 | 2770 | 175 |
| Wet deposition (Tg $yr^{-1}$) | 922 | 926 | 810 | 115 | 822 | 777 | 45 |

867
868

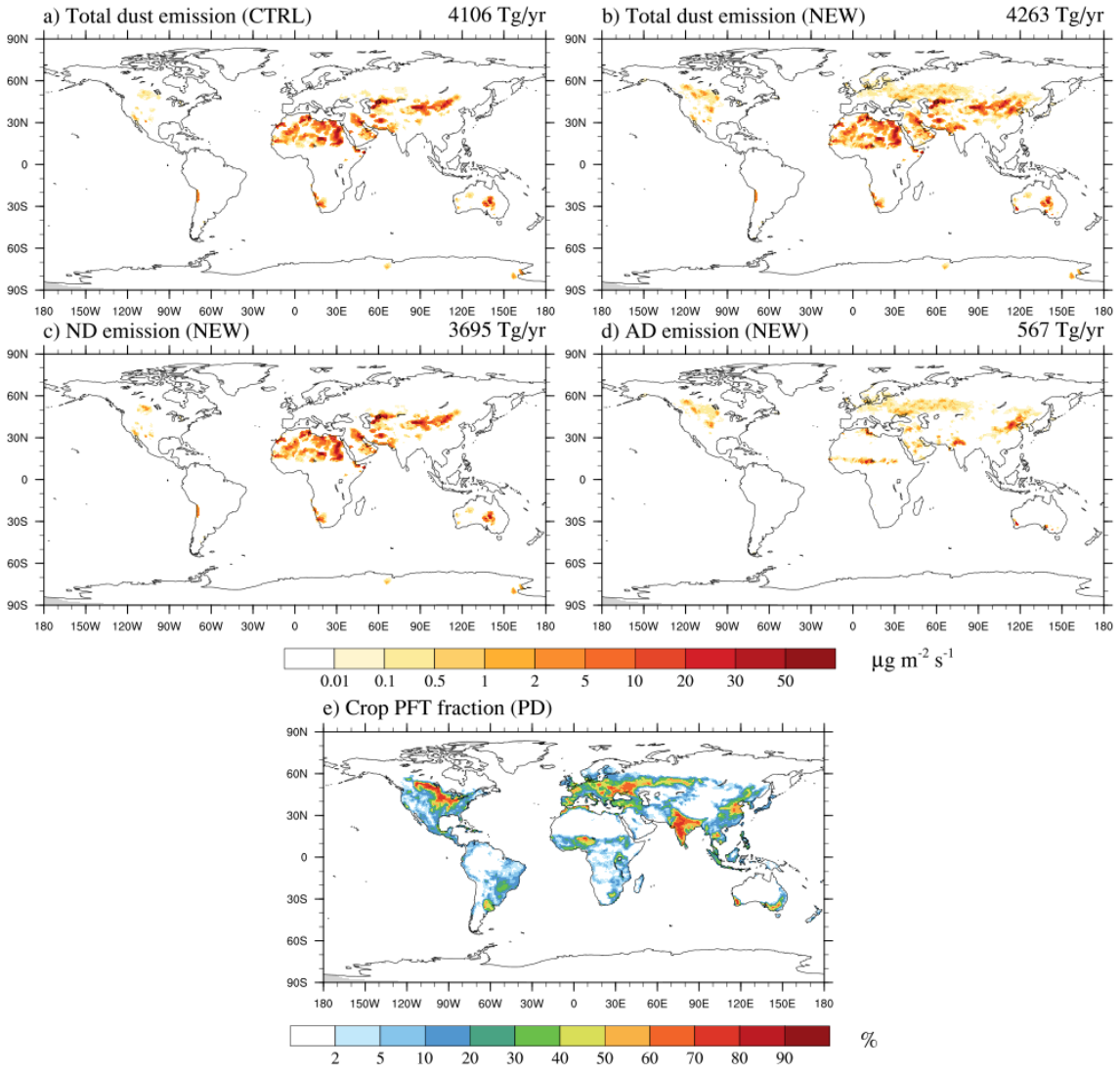


869

870 **Figure 1.** Spatial distribution of annual mean dust emission fluxes in the PD conditions.
871 Panel a) and b) shows the total dust emission fluxes from CTRL and NEW experiments,
872 respectively. Panel c) and d) shows the ND and AD emissions from the NEW
873 experiment, respectively. The numbers in panel a)-d) are total global dust emission
874 fluxes. The percentage fraction of crop PFT on each grid cell used is shown on panel e),
875 which is the same in CTRL and NEW experiments.

876

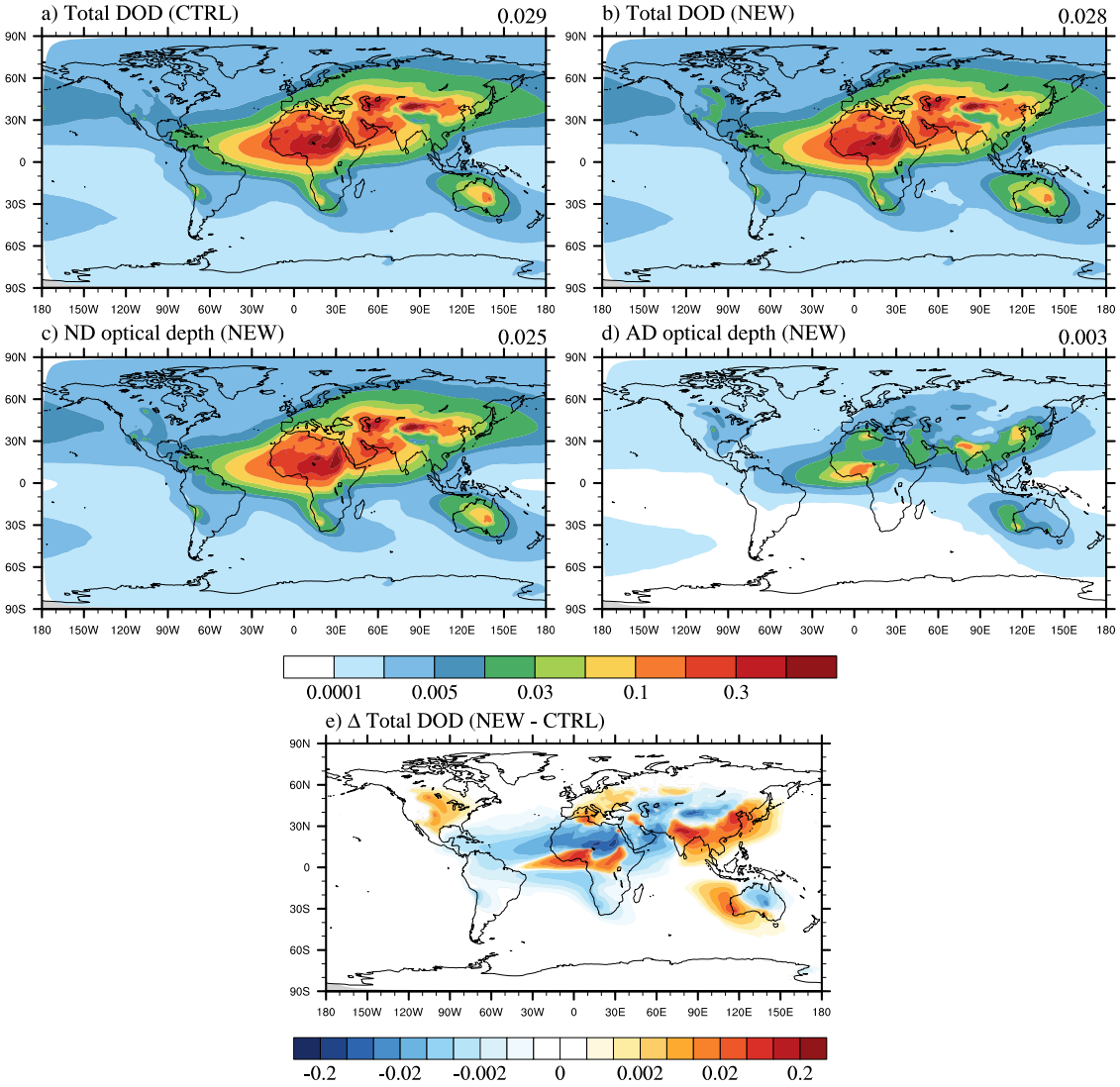


877

878 **Figure 2.** Spatial distributions of global annual mean DOD in PD condition. Panel a)
879 and b) shows the total DOD from NEW and CTRL experiments, respectively. Panel c)
880 and d) shows the ND and AD DOD from NEW, respectively. Panel e) denotes the total
881 DOD difference between NEW and CTRL. The numbers on panel a) to d) are global
882 averaged DOD.

883

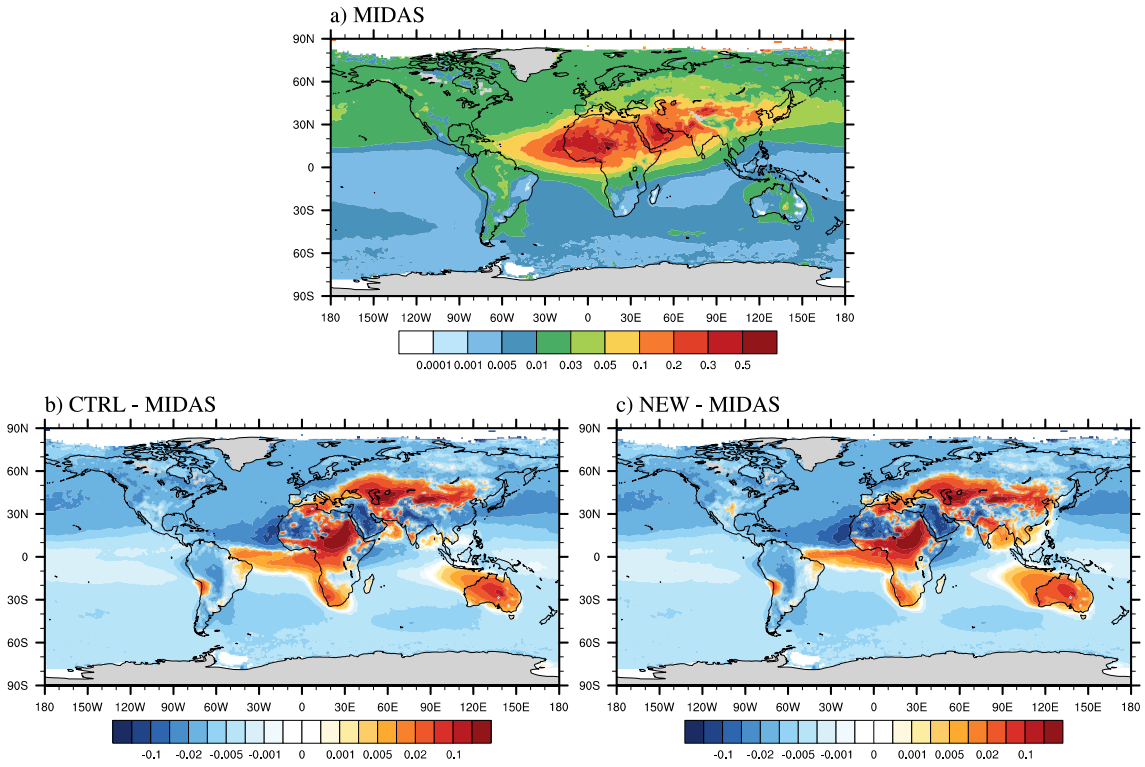


884

885 **Figure 3.** Comparison of simulated DOD with the MIDAS dataset. Observations are
886 shown in Panel a). Panel b) and c) show the differences between CTRL and NEW
887 experiments and MIDAS dataset, respectively.

888

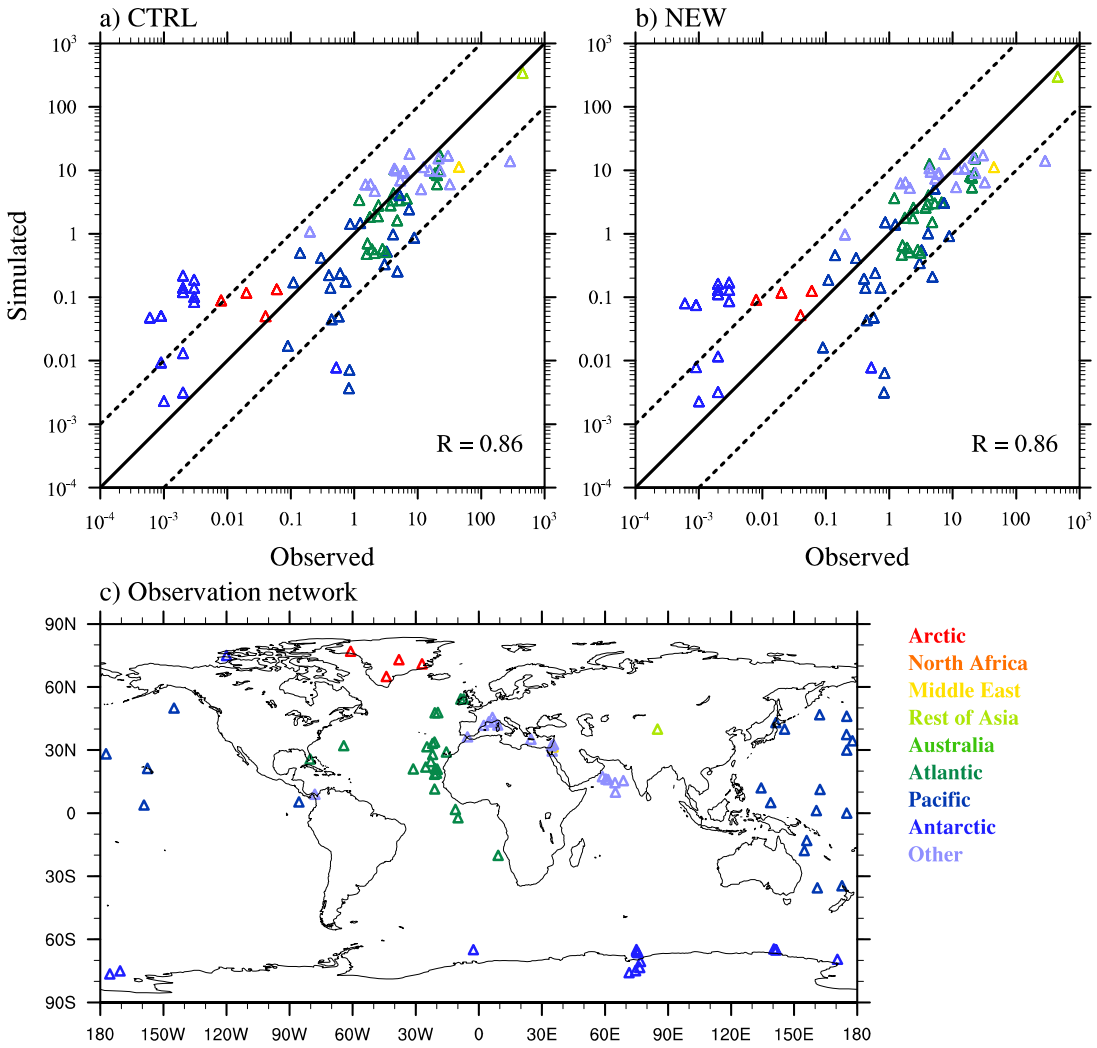


889

890 **Figure 4.** Comparisons of observed dust deposition fluxes with modeling results from a)
891 CTRL and b) NEW. Solid lines represent 1:1 comparison, while dashed lines represent 1
892 order of magnitude differences. The correlation coefficient (R) is shown on each
893 comparison. The locations of the measurements are shown in panel c). The stations are
894 grouped by regions using different colors.

895

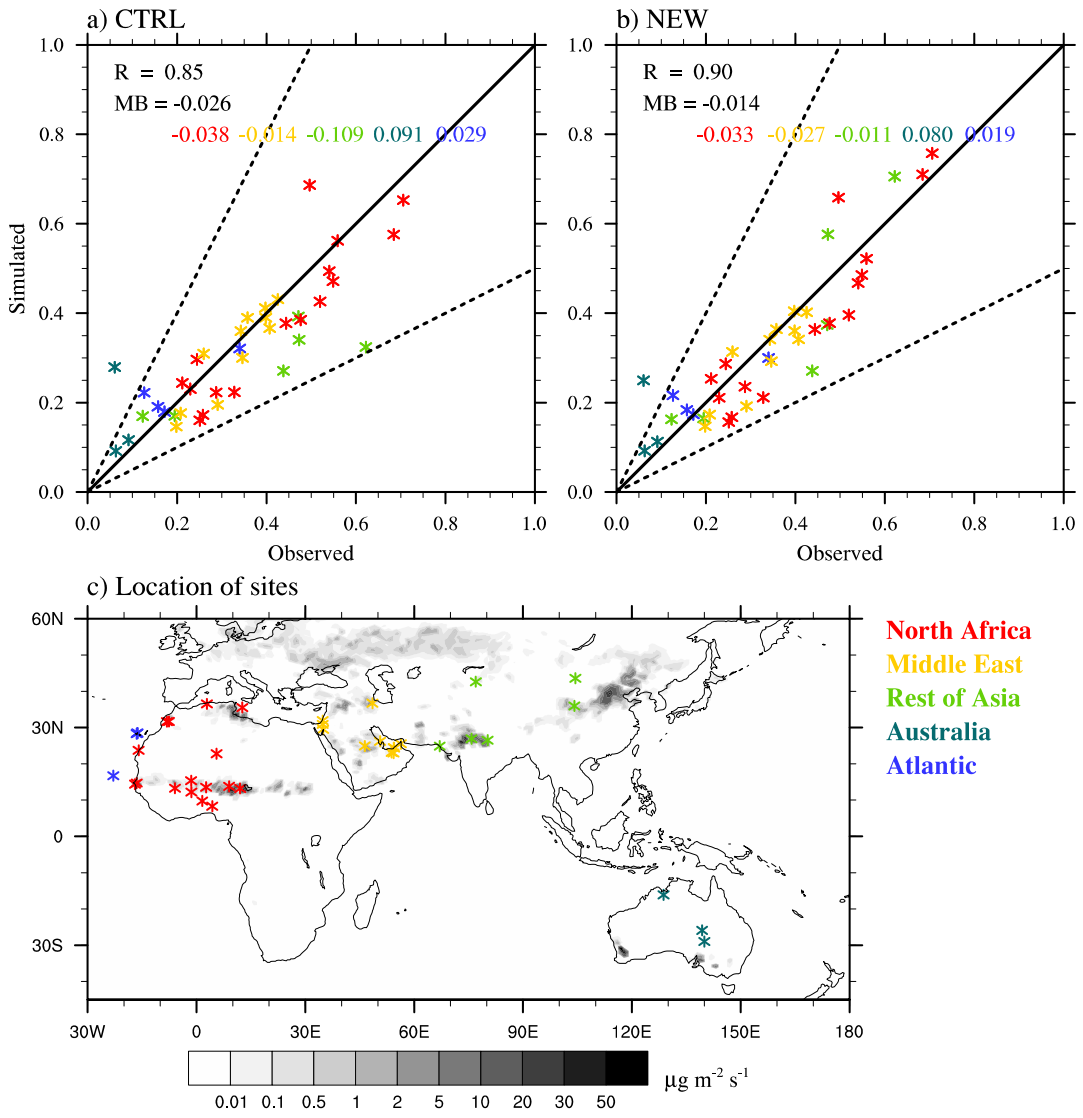


**Figure 5.** Comparisons of AERONET measured AOD and simulated AOD from a) CTRL and b) NEW experiments at 40 stations. Solid lines represent 1:1 comparison, while dashed lines mark a factor of two differences. The correlation (R) and mean bias (MB) between modeling results and observations are shown in black on the two panels. The AERONET stations are grouped regionally and classified by different colors. The MB for various regions are also shown in corresponding colors. The locations of the sites are shown in panel c). The gray contours on panel c) are the annual mean (year 2001 to 2010) simulated AD emission fluxes from NEW.

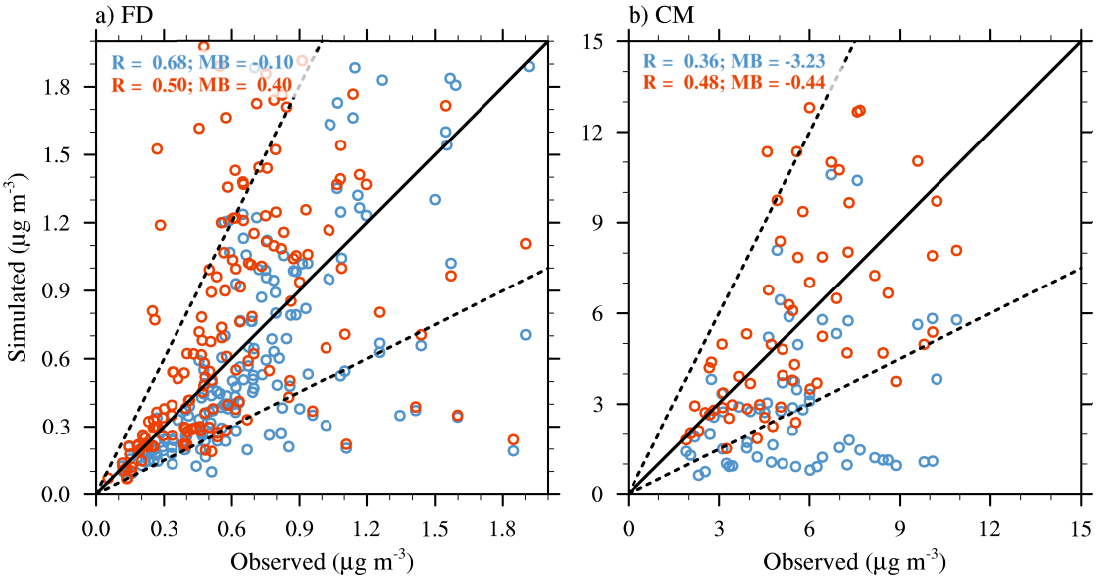


907

913 **Figure 6.** Comparisons of a) FD mass concentrations and b) CM concentrations from the
914 US IMPROVE network with modeling results from 2001 to 2010. Blue scatters are from
915 the CTRL experiment, while orange scatters are from the NEW experiment. Solid lines
916 represent 1:1 comparison, while dashed lines mark a factor of 2 differences. R and MB
917 (μg $m^{-3}$) of the comparisons are provided. The locations of the measurements are shown
918 in Figure S1.

914

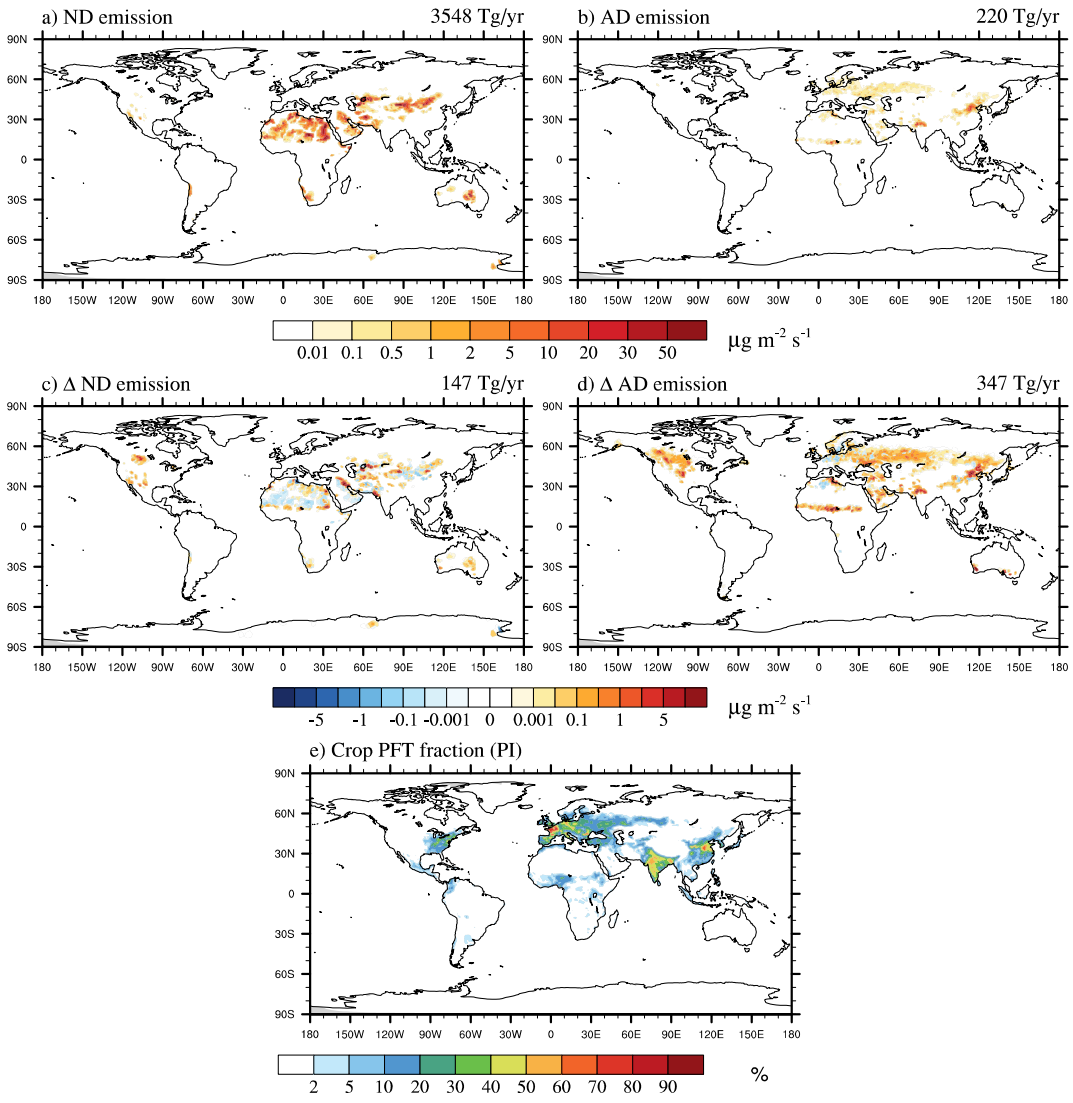


915 **Figure 7.** Spatial distribution of annual mean a) ND and b) AD emission fluxes in the PI
916 land cover condition. The differences of ND and AD emissions between PD and PI (PD
917 minus PI) land cover conditions are shown in panel c) and d), respectively. Panel e) is
918 the percentage fraction of crop PFT on each grid cell in PI. Results from NEW_PI and
919 NEW are used for the PI and PD land cover conditions, respectively.

920

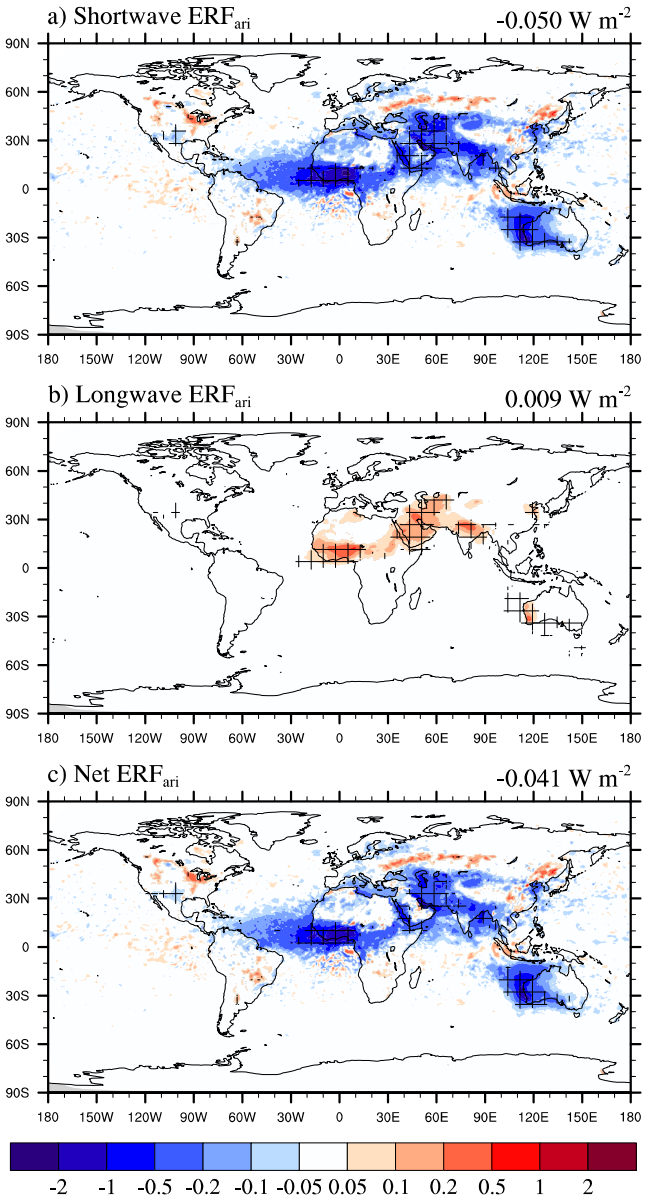


92

922 **Figure 8.** Spatial distribution of annual mean all-sky TOA a) shortwave, b) longwave,
923 and c) net ERF$_{ari}$ of dust due to the land cover change from PI to PD. Hatching indicates
924 regions where the changes are significant to the 0.05 levels.

925

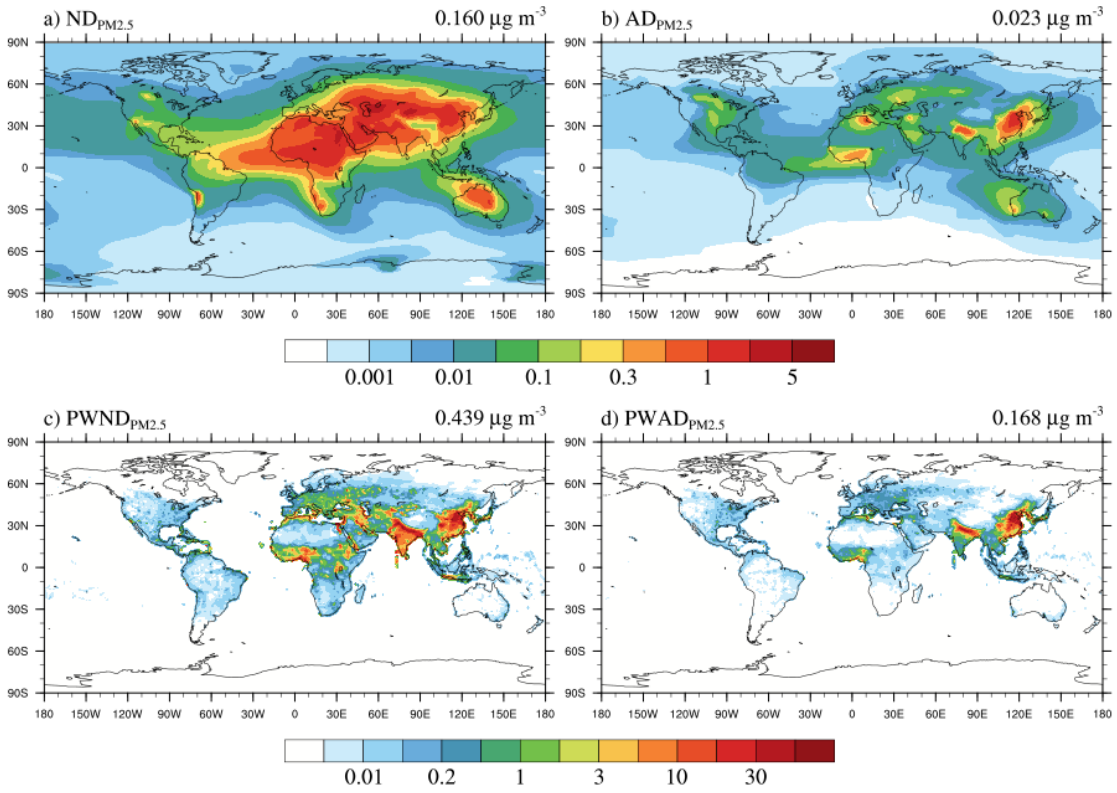


**Figure 9.** Global distribution of a) ND ($ND_{PM2.5}$) and b) AD ($AD_{PM2.5}$) surface mass concentrations in the PM2.5 size range. Panel c) and d) are the population weighted surface mass concentrations for ND ($PWND_{PM2.5}$) and AD ($PWAD_{PM2.5}$). Results from the NEW experiment are used in this figure. $PWAD_{PM2.5}$ ($PWND_{PM2.5}$) is determined through multiplying the surface mass concentration of AD (ND) in the PM2.5 size range at each grid cell with a population weight factor, which is equal to the population density at that grid cell divided by globally averaged population density. The population density data used here is the data for year 2010 from the Gridded Population of the World, Version 4 dataset (SEDAC, 2022). The resolution of this dataset is 1°, which is compatible with the horizontal resolution of our model grid.